of speckles in the *effective* detector area, assumed to be approximately two pixels along the serial transfer direction and one pixel along the parallel transfer direction of the CCD, using $R_d = 1.04$ m is $N_s = 0.35$! Thus the speckles are much larger than the detector area. One would expect a contrast of 0.82 for this measurement. The measured contrast is a factor two lower than expected. This is consistent with the results of Fraunhofer diffraction of the pinholes found in Fig. 4.4 and 4.5. For example, the fringe contrast is lower than expected in Fig. 4.5. Some loss of contrast could be due to the longitudinal coherence condition (See Fig. 2.6). For a semi-infinite crystal, a small fraction of the scattered intensity will come from the bulk of the crystal below one X-ray absorption depth. For these X-rays, the longitudinal coherence condition will not be met, thus reducing the contrast. Finally for large pinhole diameters, one would expect the spatial structure on the incident beam in Fig. 4.7 to affect the spatial coherence of the beam.

One should note that the speckle pattern contrast in Fe_3Al $(\frac{1}{2}, \frac{1}{2}, \frac{1}{2})$ is comparable to the one measured in Cu_3Au. We measured recently a contrast of 0.36 for a static speckle pattern of Fe_3Al generated with nearly ideal coherent illumination [88].

5.2 Ordering kinetics of an order-disorder phase transition

The data presented next will cover quenches performed at X25 and CHESS. Two sets of experiments were performed at X25: the so called run 21, obtained with a collimating pinhole diameter $D = 7.5$ μm and an exposure time $\tau = 120$ s, and run 24 obtained with $D = 15$ μm and $\tau = 60$ s. To test the beam stability, we also performed an experiment with the sample at $T = 300$ K, where the domains are frozen using the same parameters as run 21. At CHESS, run 113 was obtained with $D = 7.5$ μm and $\tau = 114$ s. These experimental conditions are summarized in table 5.1.

Fig. 5.10 shows the data for three subsequent times after the quench in run 21. The data are displayed with a linear grey scale between 0 and 35 counts/120s, and scaled to a synchrotron ring current of 200 mA. For $t = 50589$s, the maximum intensity

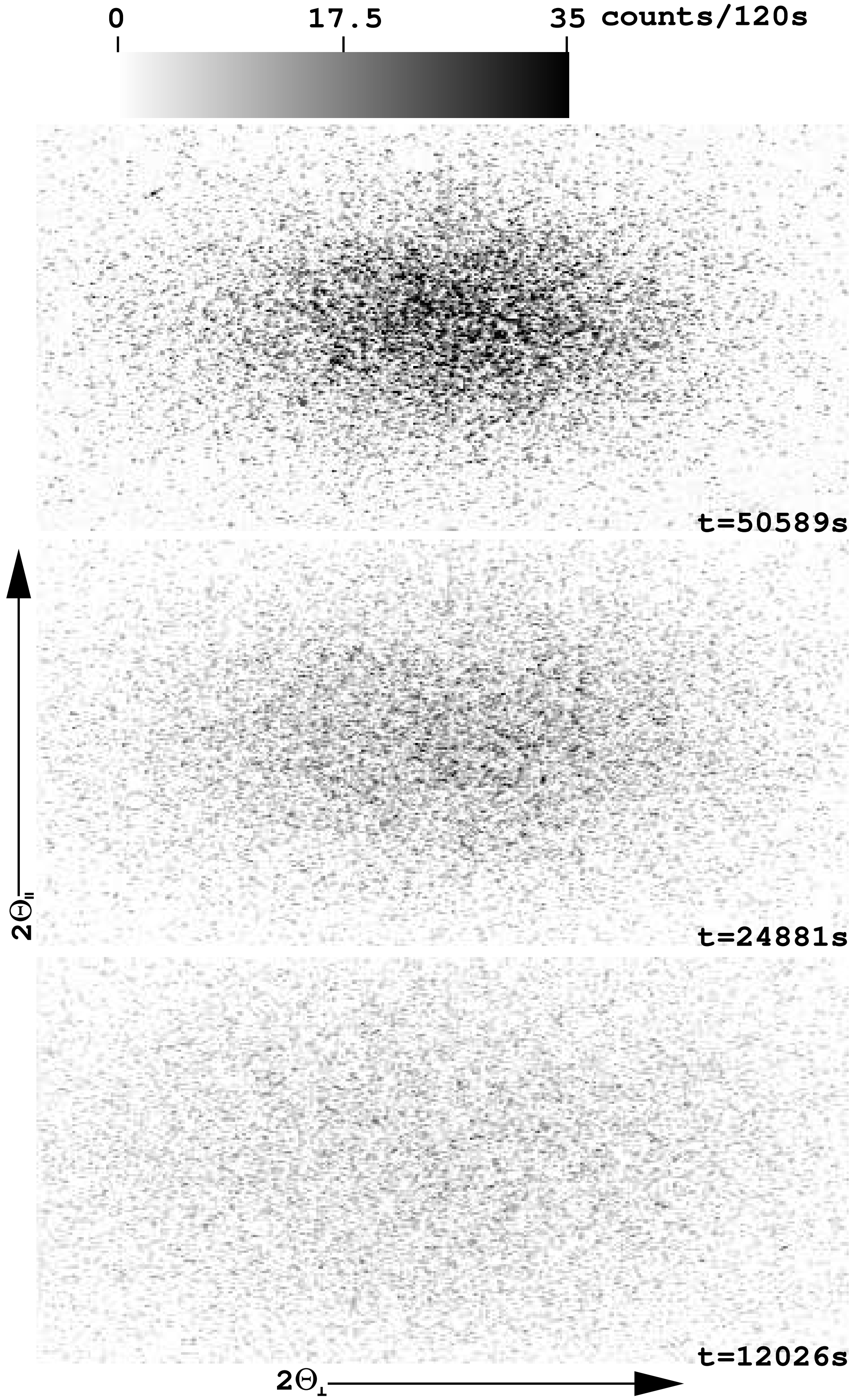

Figure 5.10: $S(\vec{q},t)$ for $t = 1.2, 2.49, 5.06 \times 10^4$ s after the quench for run 21. The data are displayed with a linear grey scale shown above. The data span a wavevector range from the center of an image of ± 0.0136 and ± 0.00678 Å^{-1} along $2\theta_\perp$ and $2\theta_\|$ respectively. As the domains grow in time, the superlattice peak intensity increases and the peak becomes narrower in reciprocal space.

Table 5.1: Summary of the experimental parameters for different experiments. The cycling time Δt is the sum of the exposure time τ and the dead time. The experiments at X25 were performed with wide open upstream horizontal slits to optimize the scattered intensity. The contrast dependence on the sample temperature and pinhole diameter is also shown. It was calculated using Eq. 5.10 over a square of 20×20 pixels centered at $\Delta 2\theta_{\perp} = \Delta 2\theta_{||} = 0$. The contrast is temperature independent for the temperatures studied in Cu_3Au.

Experiments	τ (s)	Δt (s)	D (μm)	T (K)	Contrast
Run 22	120	135.3	7.5	300	0.262 ± 0.005
Run 21	120	135.3	7.5	643	0.26 ± 0.01
Run 24	60	75.4	15	643	0.166 ± 0.006
Run 113	114	120.6	7.5	643	0.27 ± 0.01

detected is 78 counts/120s, but less than 2 % of the pixels have a count rate exceeding 35 counts/120s. These pixels are also displayed in black. Slices along $2\theta_{\perp}$ and $2\theta_{||}$ are shown in Fig. 5.11 for these three different times. As expected from the coarsening of domains, the Bragg peak sharpens along $2\theta_{\perp}$ and $2\theta_{||}$, and the peak intensity increases monotonically with increasing time. The solid lines in Fig. 5.11 are least-squares fits to a Gaussian defined by

$$S_f(\vec{q},t) = I_{max}(t) \exp\left(-\frac{(q_{\perp} - Q_{\perp}(t))^2}{2\sigma_{\perp}^2(t)} - \frac{(q_{||} - Q_{||}(t))^2}{2\sigma_{||}^2(t)}\right), \tag{5.11}$$

where $I_{max}(t)$ is the time dependent fitted peak intensity and $Q_{\perp}(t)$ and $\sigma_{\perp}(t)$ are the fit center and width along $2\theta_{\perp}$. These least-squares fits were performed on an area covering a large fraction of the two-dimensional data set[1]. These fits were used to estimate the incoherent structure factor and to give a smooth average of the structure factor which could then be used in the measurements of the time fluctuations. Note that an elliptical average of the structure factor with respect to the center of mass could also have been used to define a local average. We chose the fits because they have no random spatial fluctuations.

[1] The two-dimensional data set was fitted using a standard non-linear fitting routine, transforming the data into a one dimensional vector and using the independent coordinate to encode the position of the pixel on the CCD. Typically, a rectangular region of the CCD with 220 by 360 pixels was used along $2\theta_{||}$ and $2\theta_{\perp}$ respectively. The data were equally weighted for the fit. A small region surrounding the parasitic peak was discarded because it dominates the scattering at early times.

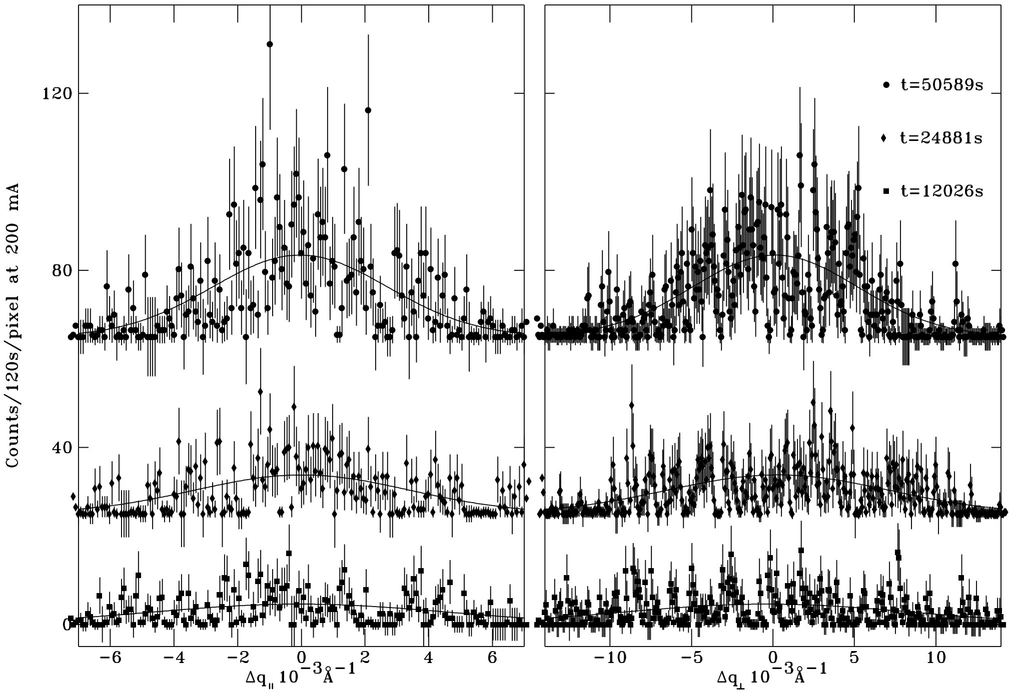

Figure 5.11: Slices of $S(\vec{q},t)$ along $2\theta_{\perp}$ and $2\theta_{\parallel}$ for the three different times in Fig. 5.10. To distinguish the data sets, a constant of 25 and 65 counts/120s was added to the data at time $t = 24881s$ and $t = 50589s$ respectively. The solid lines are least-squares fits introduced in Eq. 5.11. These fits are used as a local average for the spatial and temporal fluctuations.

Fig. 5.12 shows the time dependence of the five fit parameters for the data. The peak intensity I_{max} at the end of run 21 is 88 % of I_{max} for run 22. The peak intensity of run 24 is approximately seven times larger than for run 21, and its calculated integrated intensity is approximately five times larger than run 21 at the same time after the quench. The CHESS data are nearly 3.5 times more intense than run 21, and for an identical beam current of 200 mA, run 113 is seven time more intense than run 21. Note that an undulator was used at CHESS rather than a wiggler, and that the CHESS synchrotron ring energy is twice that of the NSLS ring.

In Fig. 5.12, the time average[1] of the fit center along $2\theta_{\perp}$ is $<Q_{\perp}>_t = 209.1 \pm 7.6$, 199.5 ± 0.6, 198.8 ± 3.4, and 242.8 ± 2.7 pixels for run 21, 22, 24, 113 respectively. A motion of one pixel is equal to an angular motion of ≈ 22 μrad. The fit center is most stable for run 22 at $T = 300$ K. During run 21, $Q_{\perp}$ drifts by twenty pixels, or

[1]The early changes in the fit parameters before $t \approx 2000$ s were discarded from the time average because the scattering is weak at early times resulting in poorer fits. The error bars quoted are the standard deviation of the fit parameters.

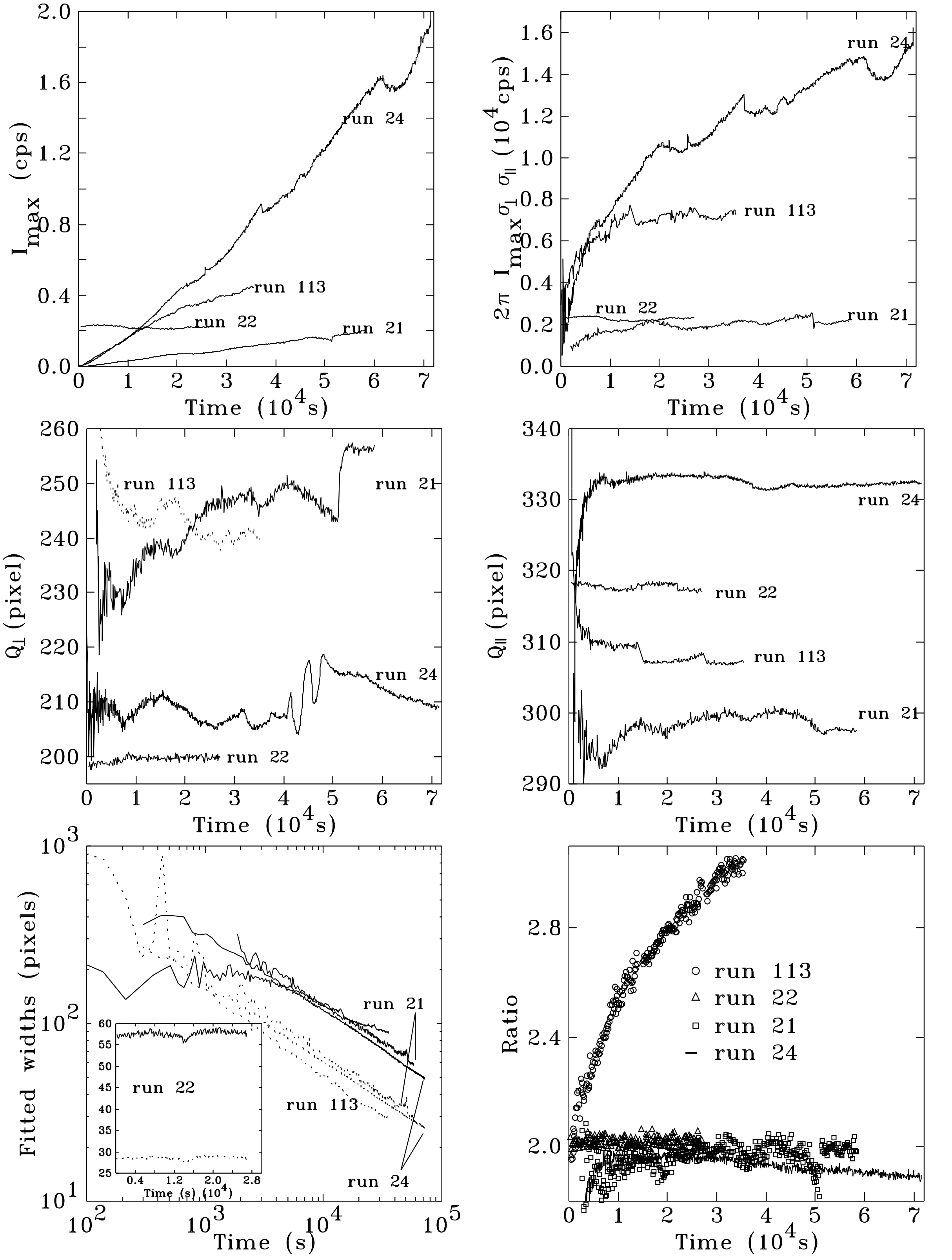

Figure 5.12: (Top left) The fitted peak intensity I_{max} for the experiments at X25 and CHESS. The CHESS and X25 data were scaled to a ring current of 100 and 200 mA respectively. (Top right) The calculated integrated intensity. (Middle left) The fit center $Q_\perp$. The data for run 24 and run 21 were offset by ten and thirty five for clarity. (Middle right) The fit center $Q_\parallel$. (Bottom left) The fitted widths $\sigma_\perp$ and $\sigma_\parallel$ are shown respectively with solid and dotted lines. The inset shows the widths for run 22 on a linear scale. (Bottom right) The ratio $\sigma_\perp/\sigma_\parallel$.

approximately 0.4 mrad, while $Q_\perp$ changes abruptly after a monochromator tweak at $t = 5.11 \times 10^4$ s. For run 24, some oscillations are seen near $t = 4.1 \times 10^4$ s. These oscillations correlate with the beam position monitor.

The time averages of $Q_{||}$ in Fig. 5.12 are $<Q_{||}>_t = 298.2 \pm 1.8$, 317.8 ± 0.4, 332.3 ± 1.4, and 308.2 ± 1.4 for runs 21, 22, 24, 113 respectively. It is most stable for run 22. The steps seen in $Q_{||}$ for run 113 are slight motions occurring after a new synchrotron fill at CHESS. The fit center $Q_{||}$ tends to be more stable than $Q_\perp$ for all the experiments reported at CHESS and X25. Since $2\theta_\perp$ is measured in the horizontal plane, the fact that the motions are greater along $2\theta_\perp$ may be due to larger incident beam motion horizontally than vertically[1].

As expected from the domain coarsening in the late time regime, the widths of the (100) in Fig. 5.12 follow a power law in both directions. For run 21, a fit of the widths to a power law, $\sigma(t) \propto t^{-n}$, yields $n = 0.43 \pm 0.01$ and 0.45 ± 0.01 for $\sigma_\perp$ and $\sigma_{||}$ respectively. For run 24, $\sigma_\perp \propto t^{-(0.41\pm0.01)}$, and $\sigma_{||} \propto t^{-(0.438\pm0.005)}$. The fitted widths along $\sigma_\perp$ are less reliable at early times for runs 21 and 24 because $2\theta_\perp$ was aligned on the serial transfer direction of the CCD. The fit becomes poorer at early times because a large fraction of the scattered intensity is outside the detector window, and count rates are low. As seen in Fig. 5.12, the ratio of $\sigma_\perp/\sigma_{||}$ is approximately two for the data recorded at X25, and it is weakly time dependent. This weak time dependence implies that the difference in the exponent of the power law for $\sigma_\perp$ and $\sigma_{||}$ is significant. For run 113, the time dependence of the ratio is caused by a temperature drift of the sample of 5°C over the total time of the experiment[2].

The expected growth exponent for Cu_3Au is 1/2 [29, 31, 32, 33], thus our measured exponents are slightly below the exponents observed by others. The coarsening dynamics are slower along $2\theta_\perp$ for all the experiments performed. Previous work reported the same exponents in both directions. Since this experiment was optimized

[1] At X25, it was observed that vertical motion is more constrained than horizontal motion because the two monochromator crystals are set to diffract at a given wavelength and a narrow range of incident angle [50]. A horizontal motion is not affected by such constraints.

[2] This temperature drift was measured in the second thermocouple used to record the sample temperature (See section 4.8).

to measure intensity fluctuations, and not growth exponents, these differences are not really surprising. It is possible that some residual non-linearities of the detector could slightly change these exponents. These fit parameters along with the contrast discussed next in table 5.1 describe the spatial dependence of the structure factor.

The time dependences of runs 24 and 113 are not shown here because they are quite similar to the ones shown in Fig 5.10 and 5.11 for run 21. Run 113 and run 21 have identical contrast within error (see Table 5.1). The main difference between the data for run 21 and run 24 is a difference in contrast due to the different pinhole diameters used. The contrast is temperature independent within error for runs 21 and 22 since they have the same D. Furthermore, the contrast measured at 300 K in Fig 5.9 using $D = 15\ \mu$m and wide open horizontal slits is 0.177 ± 0.005, in agreement with the contrast measured for run 24.

Since very little thermal diffuse scattering is observed in Cu_3Au before a quench at the annealing temperature $T = 440°$C[1], and no thermal diffuse scattering is observed above T_c as shown in Fig. 4.8, the observed contrast must be dominated by the speckle pattern created by domain walls for the observed temperature in Cu_3Au.

Fig. 5.13 shows the time evolution of a single row of the CCD in run 21 along $\delta q_\perp$ for $\Delta 2\theta_{||} = 0$. After the quench, speckles appear at fixed $\Delta q_\perp$, and their intensity grows monotonically in time. Some speckles can be seen in the figure as early as 1.2×10^4 s and remain present until 5.8×10^4 s, for a total time of over thirteen hours. The monochromator reset occurring near $t = 5.11 \times 10^4$ s affects the speckle pattern. Some speckles disappear, others appear, while some of the most intense remain present. The presence of the speckle over such an extended period was quite surprising initially. We were expecting to see dynamics with much shorter time scales than 10^4 s, as for a typical equilibrium IFS experiment. This difference between equilibrium and non equilibrium will be explained in more detail in the next section.

Fig. 5.14 shows a time series for run 22. This experiment was performed to test the

[1]Before a quench, an upper limit for the diffuse scattering at $T = 440°$C is 0.2 counts/120s/pixel at 200 mA. This upper limit is on the order of the dark pattern fluctuations.

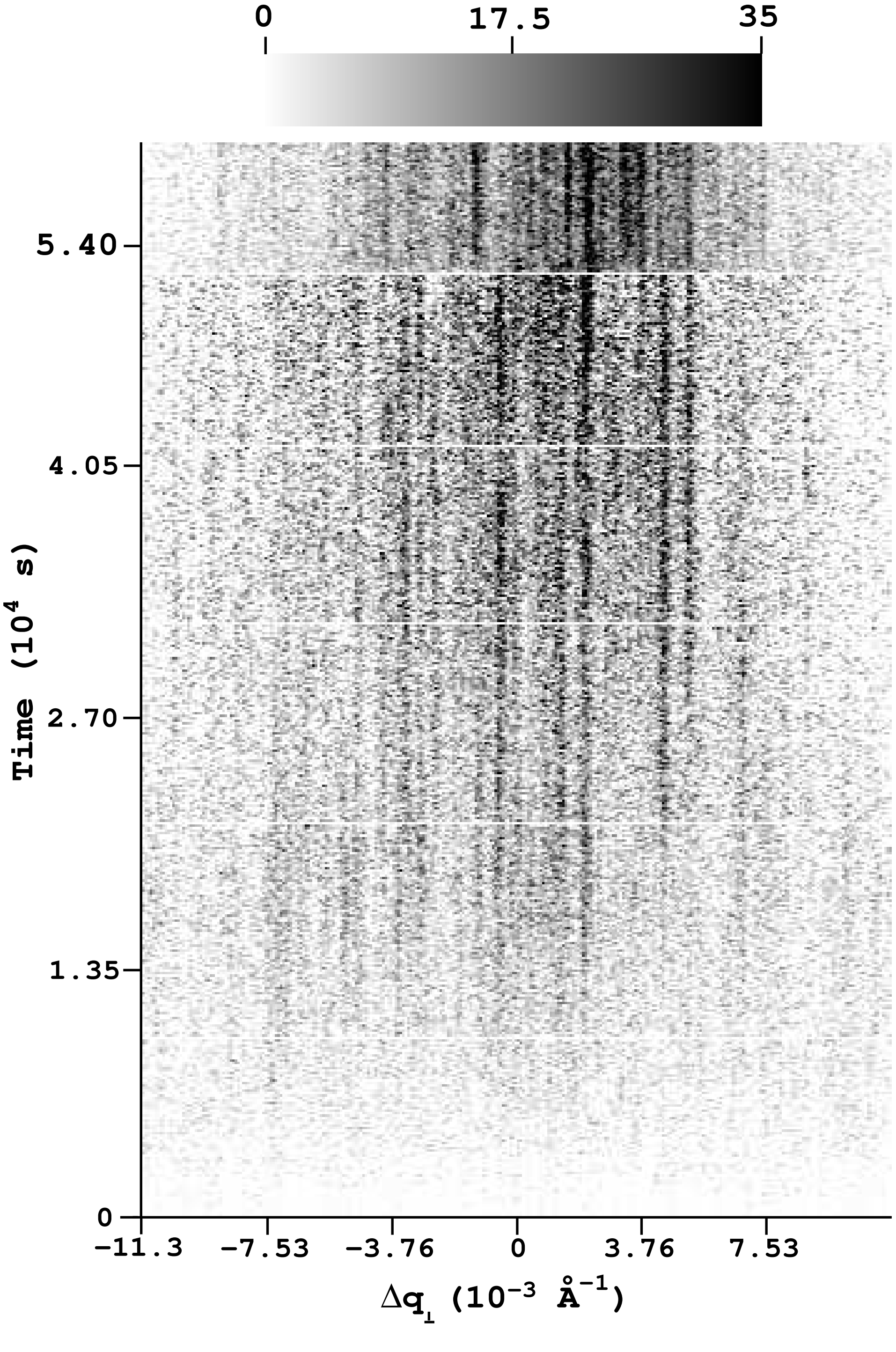

Figure 5.13: Time evolution of a single row with $\Delta 2\theta_{\|} = 0$. The grey scale displays the normalized data in counts/2min at 200 mA. The white horizontal lines are measurements of the dark pattern. The graininess on short time scales is caused by intensity fluctuations due to counting statistics. The spatial fluctuations along $\Delta q_\perp$ are speckles. After the quench at $t = 0$ s, speckles appear at fixed wavevectors, and their intensities grow monotonically. During the dark pattern at time $t = 5.11 \times 10^4$ s, the monochromator was reset. After the monochromator reset, many speckles appear and disappear.

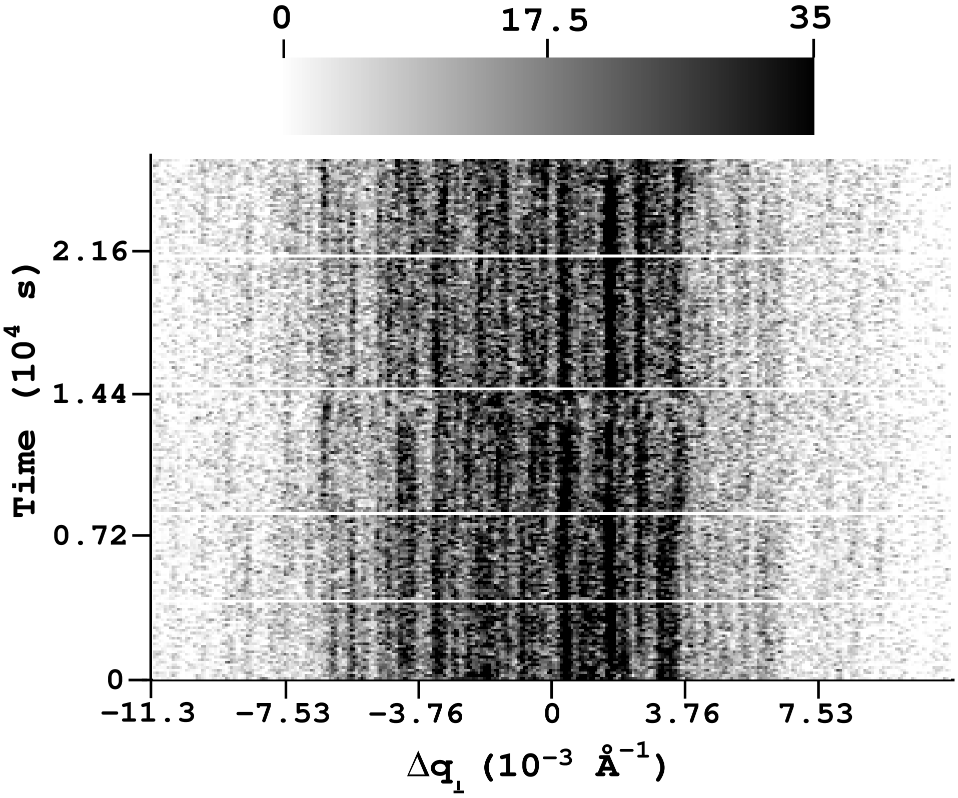

Figure 5.14: Time evolution of a single row with $\Delta 2\theta_{\|} = 0$ for run 22. The grey scale displays the normalized data in counts/2min at 200 mA. Most speckles are present over 2.6×10^4 s. Some instability is present near $t = 1.1 \times 10^4$ s. Many speckles change or move around this time. The monochromator was readjusted near $t = 2.16 \times 10^4$ s to reproduce similar conditions as run 21. The effect of the adjustment appears less pronounced than in run 21. Most speckles remain unchanged.

beam stability, since the domain motion is frozen at room temperature. Most of the speckles remain present over seven hours. Some instability occurs near $t = 1.1 \times 10^4$ s. During this time, the sample temperature fluctuated by 2.1°C over 2300s. This temperature change is caused by temperature fluctuations in the laboratory cooling water, which was used to cool the oven. A change of 2.1°C expands the Cu sample post in a direction perpendicular to the scattering plane by 2.2 μm, which is is about 30 % of the pinhole diameter used[1]. Thus, this instability could be caused by the effect of this temperature fluctuation on both the oven and on the beamline components. The monochromator was reset at $t = 2.16 \times 10^4$ s. The effect of the monochromator tweak on the speckle pattern appears less pronounced than in run 21. In run 21, we tweaked the monochromator in order to regain some incident intensity because the ratio of beam monitor to synchrotron ring current was dropping rapidly. There was no such drift in run 22.

Fig. 5.15 shows a time series of a row of the CCD with $\Delta 2\theta_{||} = 0$ for run 24. Speckles appear as early as $t = 1.44 \times 10^4$ s and some are still present after 7.1×10^4 s, or 16 hours. An instability occurs around $t = 4.1 \times 10^4$ s and lasts until $t = 4.8 \times 10^4$ s. It correlates with fluctuations of the fit center along $2\theta_\perp$ shown in Fig. 5.12. These fluctuations move the fit center by approximately ± 7 pixels, or approximately ± 150 μrad. This instability is caused by instabilities in the beamline, since these time fluctuations are also seen in a beam position monitor. Since the pinhole diameter is twice as large as in run 21, the incident intensity is larger and the relative time fluctuations on time scales of tens of minutes are smaller than in run 21[2]. The spatial fluctuations are reduced because of the smaller contrast observed (see Table 5.1). These two effects result in a smoother image than Fig. 5.13 or Fig. 5.14. Note that we tweaked the monochromator several times during this run, but no effects are noticeable on the time series. It appears that for the data collected at X25, the

[1] The Cu sample holder was 6.5 cm high. Using an expansion coefficient of 16.5×10^{-6}/K, and the quoted temperature change, one finds a motion of 2.2 μm.

[2] A careful analysis comparing the measured variance for a small number of subsequent scans $N \approx 10$ with the calculated variance expected from counting statistics calculated using the calibration curve found in Fig. 3.6 revealed that the short time fluctuations on the order of 25 min are due to Poisson noise and some incident beam fluctuations.

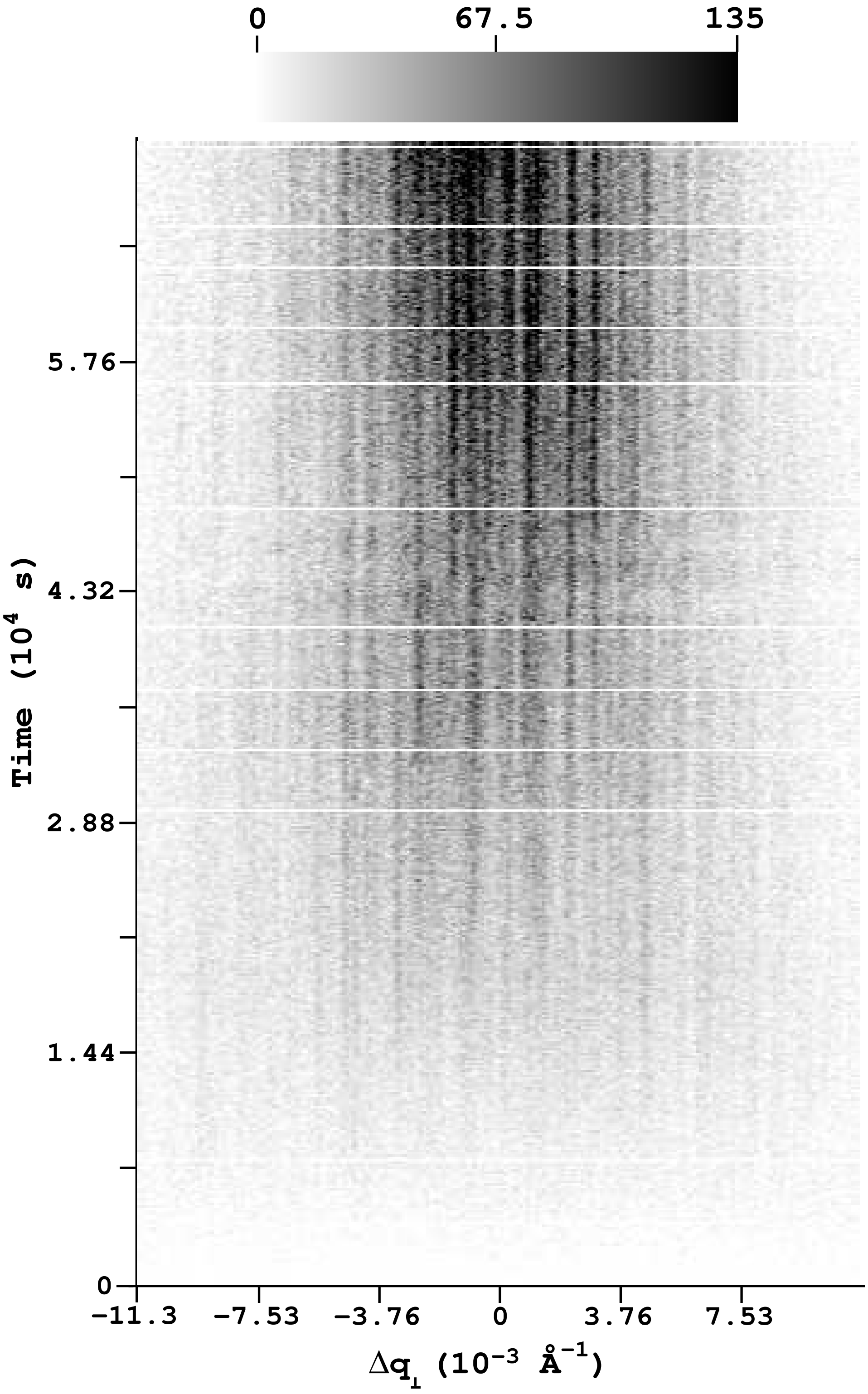

Figure 5.15: A time series of run 24, with $\Delta 2\theta_{\|} = 0$ lasting for nearly 20 hours. A linear grey scale from 0 to 135 counts/60s scaled to a maximum synchrotron ring current of 200 mA is used to display the data.

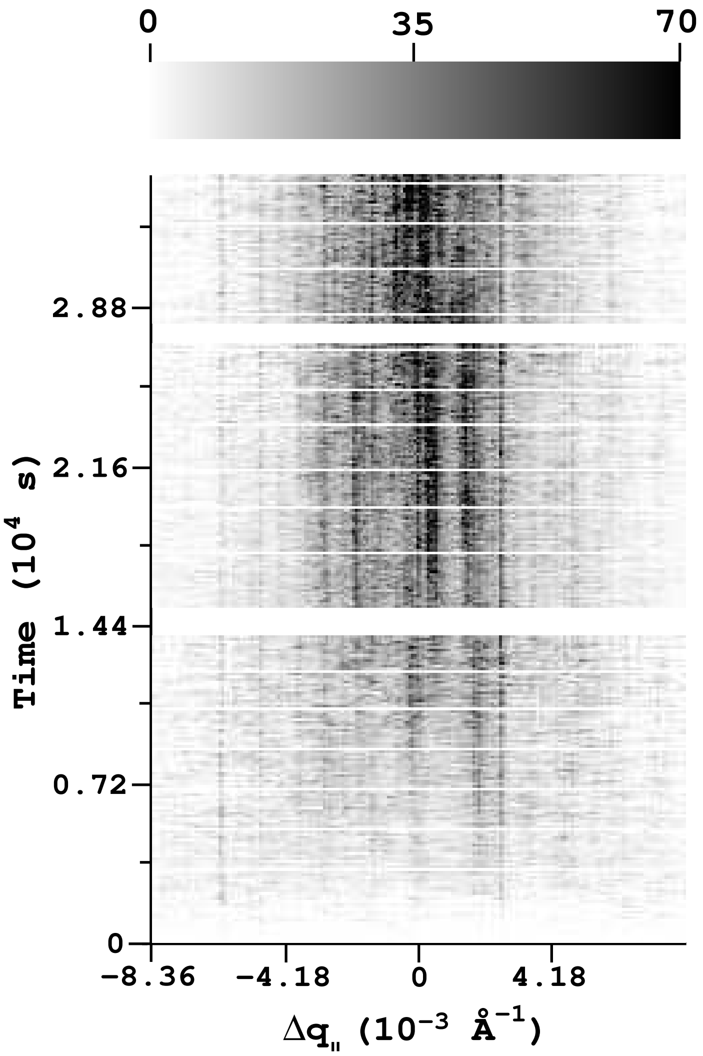

Figure 5.16: A time series of run 113. A single row of the CCD oriented for $\Delta 2\theta_{\perp} = 0$, along $2\theta_{\parallel}$ is shown. Gaps in the data occur during two synchrotron ring fills. Note that the $\vec{q}$ axis orientation of this figure is perpendicular to the previous time series shown.

speckle pattern is almost always unchanged after a monochromator reset.

Fig. 5.16 shows a time series of $S(\vec{q}, t)$ for run 113, along $\vec{q} = (q_{\parallel}, q_{\perp} = 0)$. Speckles appear as early as thirty minutes after the quench, and some of them are still present at $t = 3.4 \times 10^4$ s. The shortest fluctuation time observed in Fig. 5.16 is approximately two hours. There may be signs of faster dynamics on this data set, when compared to the data from runs 21 and 24.

To investigate in more detail the time fluctuations of $S(\vec{q}, t)$, the time dependence of the signal in several pixels is shown next for representative data sets. Fig. 5.17

shows $S(\vec{q},t)$ vs t for twenty five pixels well separated from each other in Fig. 5.13. The error bars were calculated[1] from the calibration curve in Fig. 3.6, and scaled appropriately to take into account the decay of the synchrotron ring current. The solid line is the fitted intensity $S_f(\vec{q},t)$ for the given pixels calculated from Eq. 5.11. This measurement is very different from a measurement performed with *incoherent X-rays*, where one expects the fluctuations of the data around the fit to be only due to counting statistics. The time fluctuations of the structure factor with respect to the fit are clearly above the fluctuations due to counting statistics. Note that the signal in each pixel has a *unique* random dynamics. This is what one expects in an IFS experiment. For some pixels, the structure factor remains always above or below the fit. For many pixels, the structure factor crosses $S_f(\vec{q},t)$, from values lower than S_f, to values higher than S_f at a later time. Fluctuation times range from several thousands of seconds to tens of thousands of seconds. The jump in $S(\vec{q},t)$ near $t = 5 \times 10^4$ s is due to the monochromator reset. These data are representative of the time fluctuations of $S(\vec{q},t)$ measured after a quench.

The data in run 22 were taken after run 21 to test the stability of the experiment by scattering from a sample with frozen domain dynamics. The time dependences of twenty five independent pixels in Fig. 5.14 are shown in Fig. 5.18. Apart from a random offset due to the finite contrast, the structure factor fluctuates significantly from the fit. The time fluctuations near 1.1×10^4 s are caused by the instability discussed before. Because of the presence of these time fluctuations when the coarsening dynamics is frozen, the beamline X25 did not have the time stability required at the time of the experiment[2] to clearly separate intrinsic time fluctuations of $S(\vec{q},t)$ due to the coarsening dynamics of Cu_3Au, from those caused by beamline instabilities.

[1] Given a, the ratio of the monitor count to the monitor count measured for a ring current of 200 mA, the error on the structure factor $S(\vec{q},t) = av^*(\vec{q},t)$ is $\sigma_S = \sqrt{\sigma_d^2 + a^2 1.63 v^*}$, where σ_d^2 is a dark electronic contribution to the variance measured in a region of the CCD masked by lead, and v^* is the linearized CCD signal. Here σ_S is the standard deviation of $S(\vec{q},t)$, calculated by a sum of the variances from electronic noise and Poisson noise.

[2] Since then, much work has been done at X25 to understand the long time stability of beamline X25 [50]. The instabilities seem to be caused by changes in the power loading of the monochromator due to the decay of the synchrotron ring current. Feedback techniques are under consideration to improve the long term stability at X25 [50].

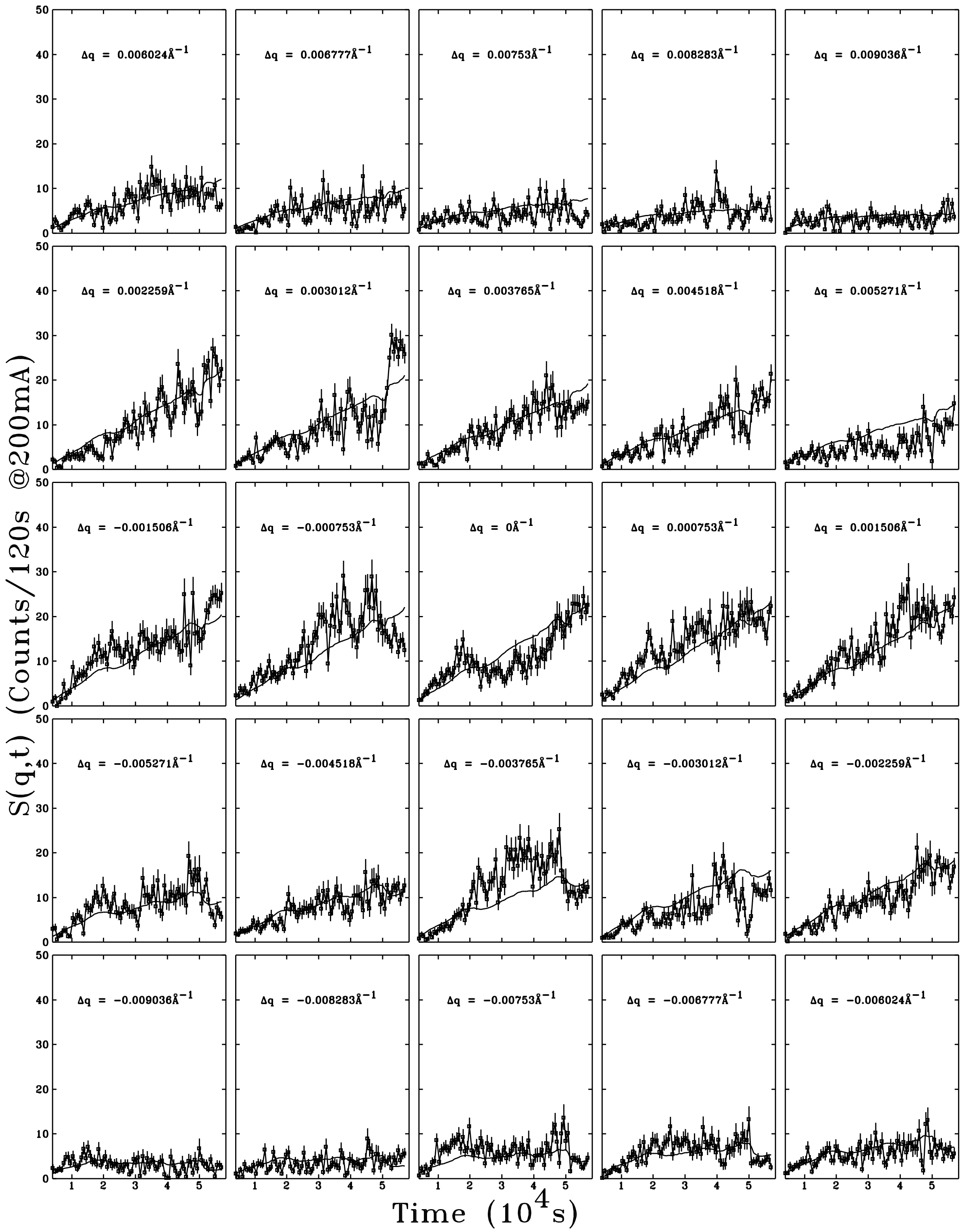

Figure 5.17: Slices of Fig. 5.13 along the time axis for run 21, with $dq_{\parallel} = 0$. Twenty five different pixels are shown, starting from $dq_{\perp} = -9.04 \times 10^{-3}$ Å^{-1} at the lower left corner, to $dq_{\perp} = 9.04 \times 10^{-3}$ Å^{-1} on the top right corner, each separated by 7.53×10^{-4} Å^{-1}. The solid line is the fitted structure factor for a given pixel. To improve the statistics, the signal was averaged in time by five scans, and in space by summing the signal from two neighboring pixels along $2\theta_{\perp}$. Each pixel behaves differently. Often, the data go from being smaller than the fit to being above it.

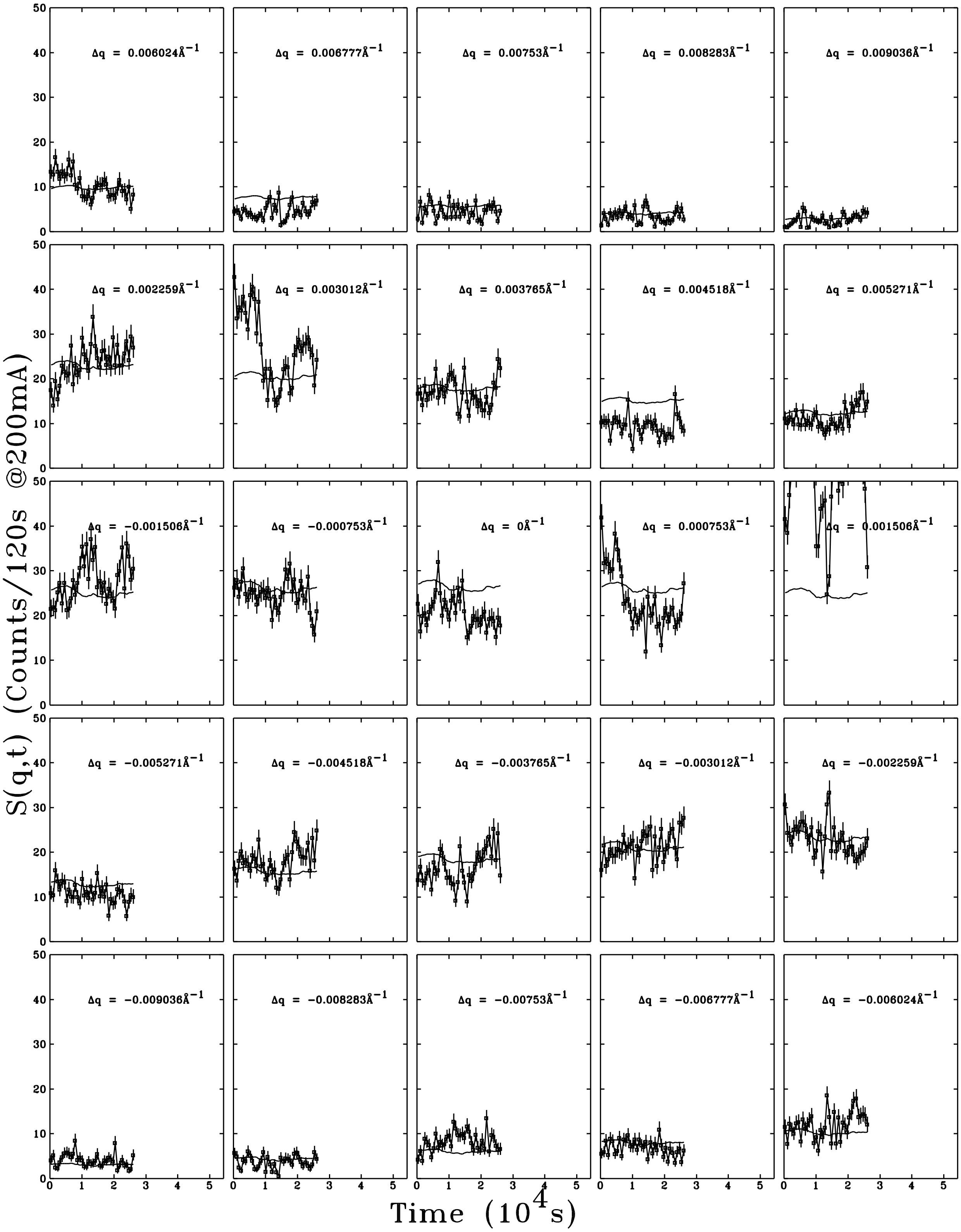

Figure 5.18: Slices along the time axis of Fig. 5.14 in run22, for $dq_{\|} = 0$. Twenty five different pixels are shown, starting from $dq_{\perp} = -9.04 \times 10^{-3}$ Å^{-1} at the lower left corner, to $dq_{\perp} = 9.04 \times 10^{-3}$ Å^{-1} on the top right corner, each separated by 7.53×10^{-4} Å^{-1}. The solid line is the fitted structure factor for a given pixel. To improve the statistics, the signal was averaged in time by five scans, and in space by summing the signal from two neighboring pixels along $2\theta_{\perp}$. Due to some instabilities, the structure factor also fluctuates significantly from the fit.

To conclude this section, we found that the measured spatial contrast for Cu_3Au (100) is temperature independent for the temperatures measured in these experiments. This shows that the speckle pattern is caused by antiphase domains, since the change in thermal diffuse scattering does not affect the contrast.

In all the experiments reported here (see Fig. 5.13–5.16), the dominant speckles appear shortly after the quench at *fixed* $\vec{q}$, and the intensity of the speckles grows monotonically in time. This is an important aspect of IFS in binary alloys out of thermodynamic equilibrium. After a quench and for a given set of initial conditions, scattering maxima appear at fixed, but random wavevectors. Different fixed wavevectors would be chosen by the system in another quench.

In the coarsening regime, the overall peak intensity of the speckle pattern grows with time, and the peak sharpens as the domains grow. A scaling function estimated by Gaussian least-squares fits of the whole speckle pattern describes well the sharpening of the structure factor. As expected, the widths along $2\theta_\perp$ and $2\theta_{||}$ are scaling approximately as $t^{-\frac{1}{2}}$.

Recall that from scaling arguments, the long time behavior of the structure factor $S(\vec{q},t) \propto R(t)^d f(\vec{q}R(t))$, where f is a scaling function, $R(t) \propto t^{\frac{1}{2}}$ is the average domain size, and $d = 3$ is the dimension of the system. An important feature of the measured speckle pattern is that it *cannot* be rescaled with such a scaling function since the speckles are fixed in reciprocal space, and any scaling function f would move individual speckles towards the center of the Cu_3Au (100) peak. Thus, the presence of speckle explicitly breaks simple scaling of the structure factor which is ubiquitous in phase transitions.

Although this appears surprising, one should recall a few important points about XIFS and scaling. The observation of speckle is a *finite size effect.* Two independent lengths scales are present here: the average domain size and the scattering volume. Strong scattering is observed in the experiment when the average domain size is a small fraction of the sample size. This strong scattering is measured at low wavevectors $\Delta q < 1/R_D$, which corresponds to the large domains. The slow dynamics of large domains explains why the individual speckles for small wavevectors change slowly in time. Furthermore, scaling in first order phase transitions implies an *ensemble average* over independent quenches or initial conditions. Here, the structure factor is calculated from a single quench! The ensemble average removes the speckles in the structure factor. These facts explain why these observations were never noted before. Note that although the speckle pattern does not follow simple scaling, the average scattering does scale as shown with the Gaussian fits. The power of XIFS is in the measurement of subtle changes of the speckle pattern. We believe that subtle time correlations of the domain structure can be obtained from a single quench on a sample size of a few μm. Much work remains to be done in this direction.

The time fluctuations of the structure factor with respect to a least-squares fit representing the sharpening of the domain distribution are clearly above counting statistics. Unfortunately as seen in Fig. 5.18, the long term stability of the experiment was not sufficient to establish whether these observed fluctuations are intrinsic to the coarsening dynamics or not. The main conclusion of this work is that the amplitude of the time fluctuations of the intensity are small, and that their time scales are very long. As shown in Fig. 2.13 and is well known from light scattering, the amplitude of the fluctuations in thermal equilibrium equals the size of the signal. If such fluctuations would have been present in this non-equilibrium experiment, they would have been easy to measure with the count rates observed.

5.2.1 Numerical Simulations of model A

The behavior described above agrees with the numerical simulation of model A. Fig. 5.19 and 5.20 show the results of a numerical simulation for three different times after a quench at $t = 0$. The parameters of the simulation were the same used in the equilibrium simulation in Eq. 2.29 with $M = -r = w = \kappa = 1.0$, with a Gaussian noise strength $2k_BTM = 0.1$ (see Eq. 2.27). The time interval between two iterations of the simulation was $dt = 0.05$, and the spatial increment $dx = 1$. The system was quenched with a random initial configuration generated with white noise ranging from -0.05 to 0.05 corresponding to the high temperature state. The images on the left

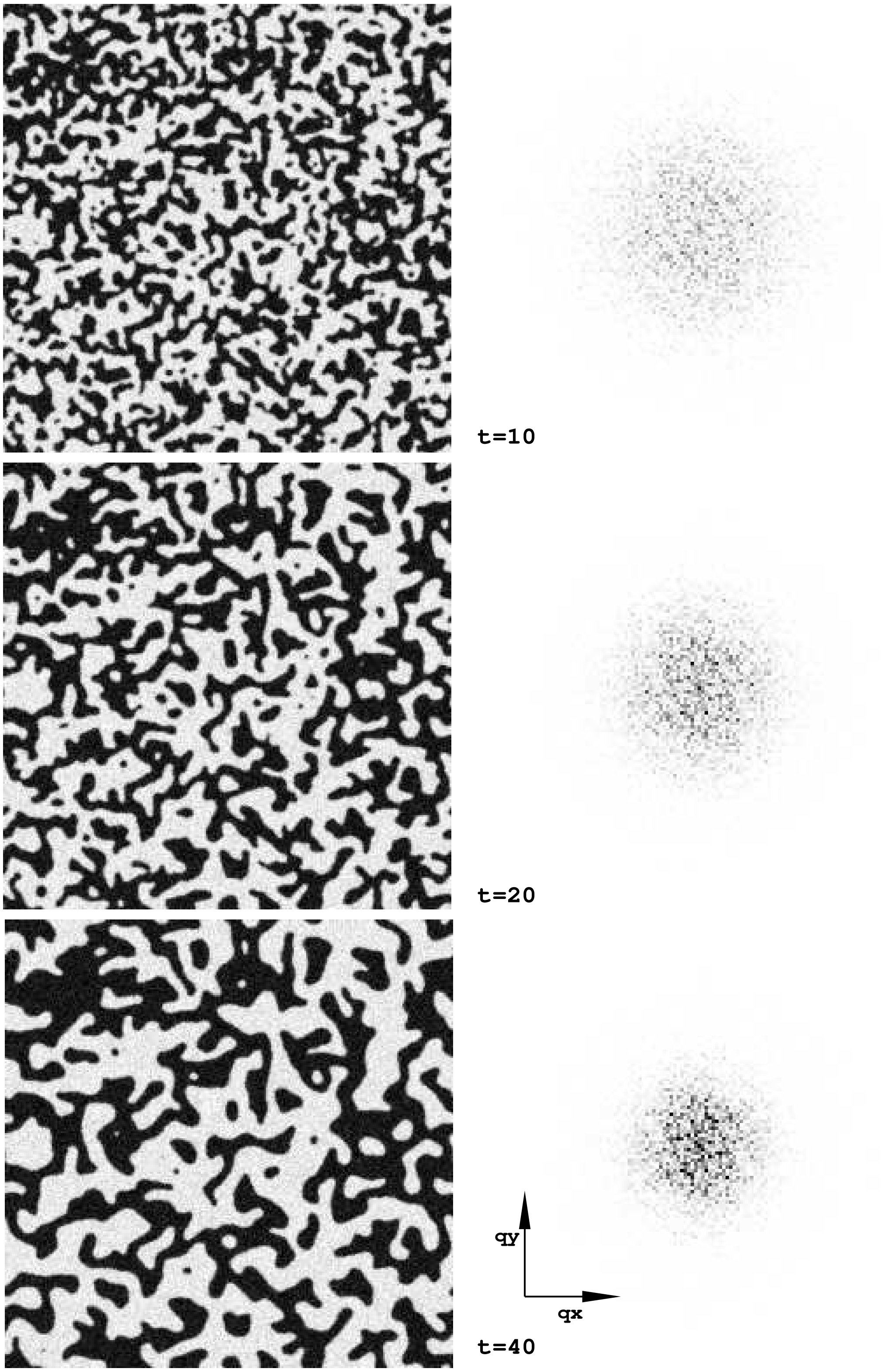

Figure 5.19: The order parameter (left) $\psi(\vec{r},t)$ and the structure factor $S(\vec{q},t)$ (right) for three different times t after the quench. A linear grey scale was used to display the order parameter from $\psi = -1.2$ (white) to 1.2 (black), and from 0 to 0.003 for the structure factor. The order parameter spatial dependence is shown for a system of 512×512. The central 128×128 elements of the structure factor are shown. The central pixel in these images corresponds to $\vec{q} = 0$. Speckle is caused by the coherent diffraction from the random domains shown. As the domains grow, the structure factor sharpens and its intensity increases.

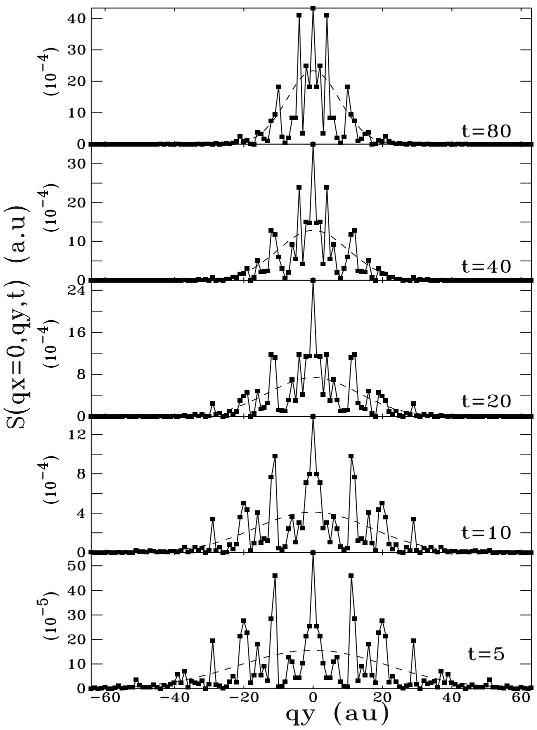

Figure 5.20: Slices of $S(\vec{q},t)$ for model A, for times $t = 5, 10, 20, 40, 80$ after the quench. The solid line is used as a guide to the eyes. The structure factor grows by a factor 8 and the peak sharpens. Most speckles remain fixed in $\vec{q}$, and their intensities fluctuate slowly. The dashed lines are fits described in the text.

in Fig. 5.19 show the time dependence of the order parameter for a simulation size of 512×512. In the coarsening regime for model A, it is well known that a simultaneous rescaling of length and time by factors of two and four respectively yields comparable domain structures [60]. In Fig. 5.19, for example, by rescaling one quarter of the 512×512 system at time $t = 10$ by a factor two, one would find that the domain structure of the rescaled system appears similar to the non-rescaled system at a later time $t = 40$.

On the right of these images, the structure factor calculated from Eq. 2.10 is shown with a linear grey scale. Fig. 5.20 shows slices of $S(\vec{q},t)$ with $\vec{q} = (0, q_y)$ and time $t = 5, 10, 20, 40, 80$. As observed in our experiments, speckle is present in the simulation. In order to reduce the speckle in the structure factor, most theoretical work performs either averages on an ensemble of independent initial conditions, or on several wavevectors with identical magnitude $|\vec{q}| = q$. By performing these averages, one looses much of the information on the fluctuations of the order parameter during

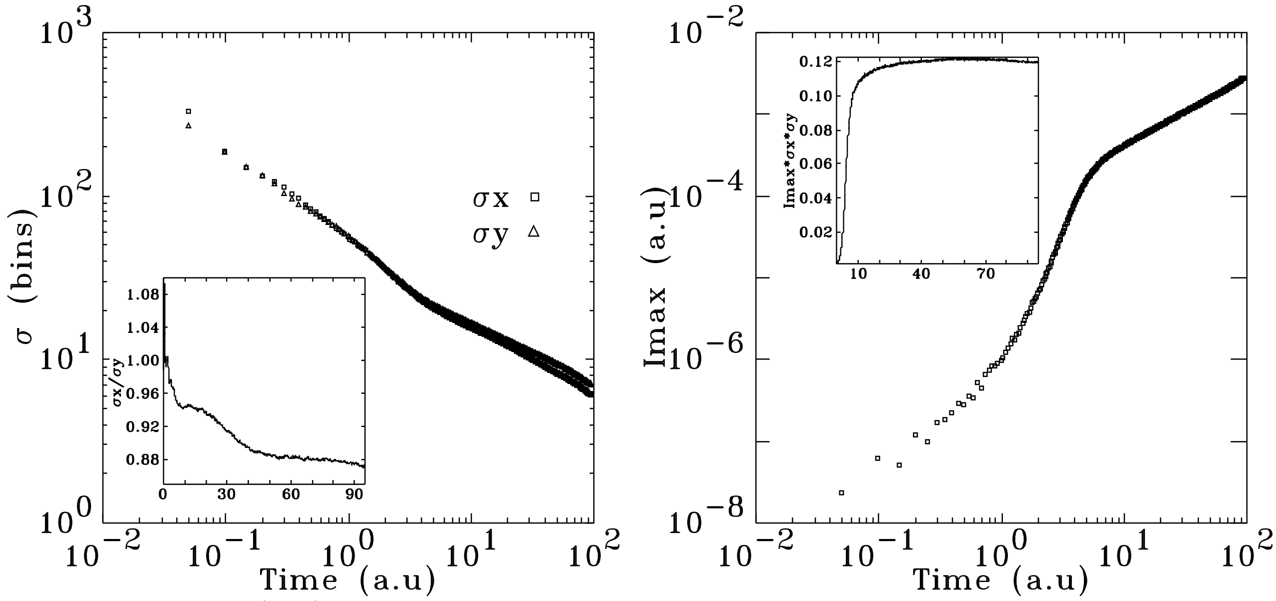

Figure 5.21: (Left) The time dependence of the two perpendicular fitted widths σ_x and σ_y. The widths are measured in units of the wavevector resolution $\Delta q = 2\pi/L$, where L is the system size. The inset shows the time dependence of the ratio of σ_x/σ_y. The ratio of the fitted widths is below unity at late times indicating a slight difference between the exponents of the widths. (Right) The peak intensity, I_{max}. After a transient, the system crosses over to scaling after time $t \approx 7$. The inset shows the integrated intensity for the fit $I_{max}\sigma_x\sigma_y$ vs time.

the quench.

The domain coarsening in Fig. 5.19 and 5.20 is seen by a sharpening of $S(\vec{q}, t)$ and an increase in the intensity of the peak. The dashed line in Fig. 5.20 is a least-squares fit of the structure factor to a Gaussian defined in Eq. 5.11. In analogy with the CCD data, this fit is used to define a local average for the fluctuations.

Fig. 5.21 shows the time dependence of the fit parameters. The center of the fit was fixed at $\vec{q} = 0$. A plot of the fitted widths σ_x and σ_y is shown. A fit of each width to a power law in the coarsening regime, i.e. from $t = 7$ to 95, gives $\sigma_x \propto t^{-0.41}$ and $\sigma_y \propto t^{-0.40}$. This difference is real since the ratio of σ_x/σ_y decreases as t increases (See the inset). It is amusing to note that these power law exponents are similar to the data.

A plot of the fitted peak intensity, I_{max}, is also shown as a function of time after the quench. The peak intensity, after a transient which last until $t \approx 7$, becomes a power law. This is consistent with the coarsening of domains. A fit of the peak intensity from $t = 7$ to 95 gives $I_{max} \propto t^{0.86}$. The inset shows the calculated integrated intensity of the fitted Gaussian $I_{max}\sigma_x\sigma_y$. It is time dependent in the nucleation regime, but slows down after $t \approx 7$. In the coarsening regime, it is slightly time dependent since the sum of the exponents from the widths and peak intensity does not add up to zero.

The magnitudes of these exponents are significantly lower than the expected exponents for model A. For model A, one expects $\sigma_x \propto t^{-\frac{1}{2}}$, $\sigma_x/\sigma_y = 1$, and $I_{max} \propto t^{\frac{d}{2}}$, with $d = 2$ dimensions. The expected results are obtained from an ensemble average of many quenches with different initial conditions, and the structure factor is circularly averaged. It is well known that one must average several quenches to get adequate statistics for these parameters. These differences in the magnitude of the exponents, and the anisotropy of $S(\vec{q}, t)$ are consistent with the poor sampling of phase space for a single quench.

Fig. 5.22 shows a time series of $S(\vec{q}, t)$ for $\vec{q} = (qx, 0)$. The time dependence is shown here for 100 wavevectors using the grey scale shown. From the definition of the structure factor, the figure is symmetric with respect to the origin $\vec{q} = 0$. Recall that the fluctuation time in equilibrium for model A is $\tau_c = \frac{1}{M(2q^2-4r)}$, which ranges from $\tau_c = 0.25$ to 0.08 as shown in Fig. 2.11c. The fluctuations on Fig. 5.22 are several orders of magnitude slower than the equilibrium fluctuations of the short range order. At low momentum transfer, the fluctuation times are much larger than the simulation time shown, but for large qx, fluctuations are observable on time scales ranging from ≈ 2 to 60, which is still much larger than τ_c. This is shown in more detail in Fig. 5.23, where slices for several qx are shown. The solid line is the simulation data, and the dashed line is the Gaussian fit, with parameters shown in Fig. 5.21. The sudden rise and decay of the fit for a given qx gives us a characteristic time for the coarsening dynamics at a given qx. For low qx from 0 to 20, the simulation time is comparable to the coarsening time, but for higher qx, some intensity fluctuations are seen above the fit with time scales of the order of $\Delta t = 20$.

The time correlation of these fluctuations has not been investigated further. More work remains to be done in this area. We urge theorists to investigate the intensity fluctuations of the structure factor without performing *spherical averages*, because it

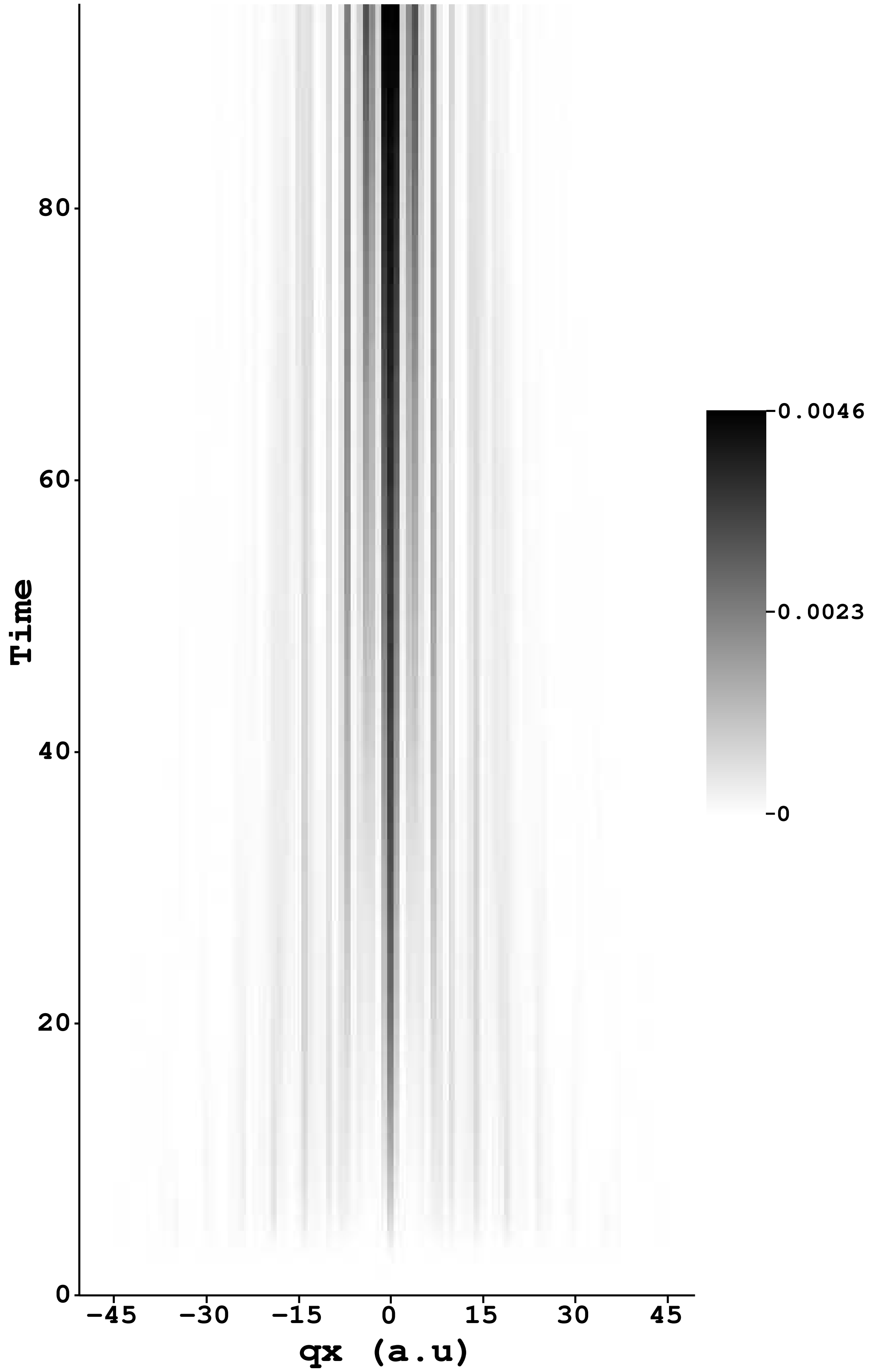

Figure 5.22: A time series of $S(\vec{q},t)$, for $\vec{q}=(qx,0)$ after a quench at $t=0$. The component qx is measured in units of $\Delta q = 2\pi/L$, where $L=512$ is the system size in Fig. 5.19. Note that a speckle at $qx=7$ has a wavelength $\lambda = 2\pi/qx = L/7$. The fluctuations of the structure factor for model A are much slower than the equilibrium fluctuations discussed in Chapter 2 because the dominant speckle correspond to the Fourier modes associated with the long wavelength domain structure in the sample. As seen in Fig. 5.19, this overall domain structure changes very slowly.

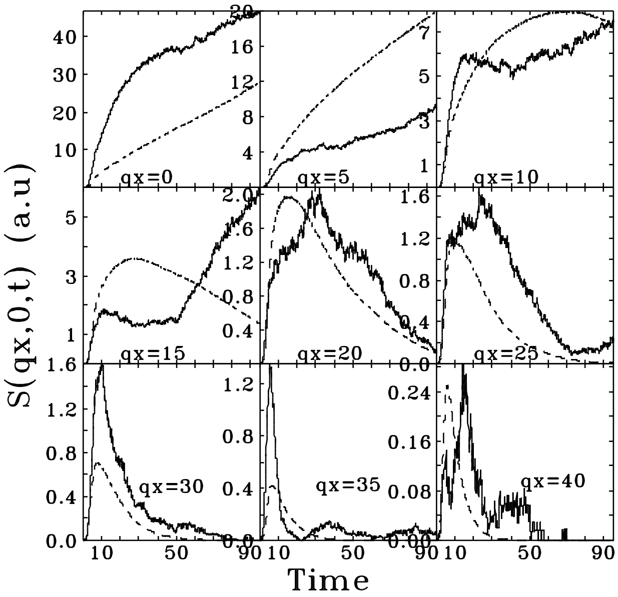

Figure 5.23: $S(\vec{q},t)$ vs t for several qx ranging from 0 to 40. The solid line is the simulation data, and the dashed line is a least-squares fit to a Gaussian discussed in the text.

is now possible to measure these fluctuations with coherent X-rays! This time correlation function should provide additional information on the dynamics of ordering.

In conclusion, we find that the numerical simulation of model A is in good qualitative agreement with the measurements in Cu_3Au. The simulation shows that the dominant speckles are fixed in reciprocal space and their intensities slowly increase in time. Fig. 5.22 shows that the long-lived speckles correspond to long wavelength fluctuations associated with the domain structure. It is clear from Fig. 5.19 that a large fraction of the overall domain structure correlates with itself at later times. This explains why the time fluctuations of the speckle pattern from Cu_3Au (100) and for the theoretical simulation are much longer than the typical fluctuation times found in equilibrium.

Note that it is not essential to use a detailed model of Cu_3Au with a more physical Hamiltonian to understand the data. The small system size for the simulation (Here 512×512) will always be much smaller than the experimental system (4.4×10^{12} unit cells!)[1]. The essential features are present in the simple model shown here. This

[1]The illuminated volume in our experiment is $D(\frac{D}{\sin\theta_B})(\mu\sin\theta_B) = D^2\mu$, where $D = 7.5$ μm is the collimating pinhole diameter, $\mu = 4.2$ μm is the absorption length of X-rays in Cu_3Au at 7 keV. Dividing this volume by the lattice cell volume (3.711 Å)^3, we find that our illuminated volume

slow dynamics of speckle after a quench from the disordered equilibrium phase to the ordered phase will be present in any model and depends only on the presence of an extended domain structure which persists over an extended time. For example, we expects the dynamics of speckle in model B to be even slower than model A, because of the smaller growth exponent in model B (1/3 instead of 1/2).

More theoretical work remains to be done to make some prediction on the time correlation function. Due to long time instabilities in the beamline at X25, these experiments should be performed again at the new third generation sources like ESRF and APS in order to study the detailed time dependence of the speckle pattern. Recently, we have demonstrated that the Troika beamline at ESRF is sufficiently stable to perform IFS on Fe_3Al near its critical point [19]. Because of the small contrast of the time fluctuations of $S(\vec{q}, t)$ in these systems, the increase in coherent flux should allow one to measure more subtle fluctuations of the structure factor.

corresponds to 4.4×10^{12} unit cells.